Mechanistic Insights on the Hydrodeoxygenation of Benzyl Alcohol with a Pd-Terpyridine Catalyst

By

Isaac Moore
B.S., Evangel University, 2019

Submitted to the graduate degree program in Chemistry and the Graduate Faculty of the University of Kansas in partial fulfillment of the requirements for the degree of Master of Science.

Chair: Prof. Marco Caricato

Prof. Brian B. Laird

Prof. Christopher Elles

Date Defended: 13 May 2022

The thesis committee for Isaac Moore certifies that this is the approved version of the following thesis:

Mechanistic Insights on the Hydrodeoxygenation of Benzyl Alcohol with a Pd-Terpyridine Catalyst

Chair: Prof. Marco Caricato

Date Approved: 13 May 2022

Abstract

Lignin is a readily available renewable carbon polymer consisting of aromatic monomers, which can be used in the generation of alternative fuels. However, many of these monomers contain oxygen, reducing their usability and overall value. Therefore, catalytic hydrodeoxygenation that allows for the removal of oxygen atoms while preserving the aromaticity of these monomers is desirable. The Vannucci group at the University of South Carolina has developed a catalyst for this purpose, chloro(2,2':6',2''-terpyridine-4'-carboxylic acid) palladium(II) chloride. Their catalyst has shown high conversion and selectivity with model lignin monomers at low temperatures when attached to the surface of amorphous silica to generate a molecular/heterogeneous catalyst motif. The two mechanisms investigated include one where the Pd center is reduced and one where an intermediate Pd-hydride species appears. In this thesis, we use density functional theory to determine the structures for the intermediate and transition state species, and their corresponding energies. With these energies, we ascertain which of the proposed reaction mechanisms is energetically favored. Understanding this mechanism and determining what leads to the high conversion and selectivity of this catalyst will help in the future development of similar catalysts with increased efficiency, conversion, and selectivity, potentially leading to a wider availability of these fuels.

Acknowledgements

First, I would like to thank my advisor, Marco Caricato, for the opportunity to work on this project and for his mentorship throughout my time at KU.

I would also like to thank the rest of my advisory committee, Chris Elles and Brian Laird, for the wisdom you have imparted to me over the past 3 years.

I would also like to acknowledge the other members of my group, Kaihua Zhang, Taylor Parsons, Brian Faintich, and Shreyaa Brahmachari, as well as former group members Dr. Ty Balduf, and Dr. Amy Jystad. The support all of you have given over the years has been invaluable, and it has been an honor and a privilege to work alongside each of you during my time at KU.

I also want to thank my undergraduate mentors, Dr. Matthew DeVore, Dr. Natasha DeVore, Dr. Don Tosh, and Prof. Dianne Twigger. My inspiration to further my education with graduate school came from the example you set for me during my time at Evangel University, and that push in the right direction has changed my life for the better.

I also wish to thank my friends, Ally Deeken-Krieg, Sahan Godahewa, and Ashley Borkowski, for providing emotional support during the process of writing this thesis. I will always cherish the random conversations we've had while mutually procrastinating.

Most importantly, I want to thank the two most important people in my life, my amazing wife Krista and our son Micah, for being there for me throughout this crazy rollercoaster of graduate school. You two are the reason I wake up every morning, and you

were the reason I kept going no matter how difficult it got. I love you both so much more than I could ever say on paper.

Table of Contents

Table of Figures

Chapter 1: Introduction

In this thesis, we investigate both reaction pathways for the hydrodeoxygenation of benzyl alcohol proposed by the Vannucci group for their Pd-terpyridine catalyst[1,2] (Figure 1.1) using density functional theory (DFT) calculations. We find the optimized structures for each intermediate geometry on both of the proposed reaction pathways to determine which one is energetically favorable. With the optimized structures for each intermediate, we also analyze why one pathway might be preferred over another.

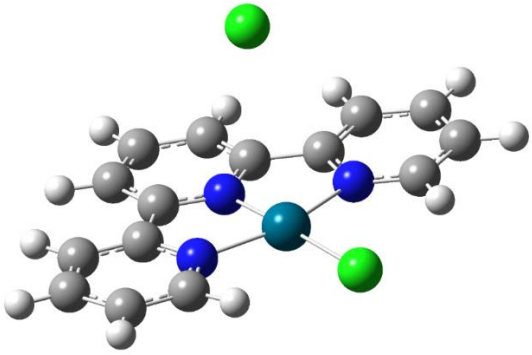

Figure 1.1: Chloro(2,2':6',2''-terpyridine) palladium (II) chloride, or Pdtpy

The Vannucci group has synthesized polypyridyl single-site catalysts with nickel and palladium for HDO of benzylic lignin monomer models like benzophenone, benzaldehyde, and benzyl alcohol.[1] These single-site molecular catalysts have shown better selectivity towards preservation of aromaticity in comparison to electrochemical and photochemical methods.[3–5] They have also found that their Pd catalyst (Pdtpy) is significantly more effective than the similar Ni catalyst they tested.[1] This complex is shown to be very effective when modeling the HDO reaction in the lignin upgrading process with benzyl alcohol used as the model bio-oil component. Further studies show their homogenous molecular catalyst at

100°C provides excellent conversion with near-perfect selectivity with methanol as the solvent. However, the same reaction is significantly less favorable at room temperature, which suggests that the use of other solvents may be preferable.

Because the catalyst complex is an ionic compound, it is necessary to use a heterogeneous catalytic motif to determine the effect of nonpolar solvents on this reaction. Therefore, the complex was attached to an amorphous silica surface by the addition of a linker COOH group attached to the pyridyl 4' carbon. This modification to the original catalyst complex geometry allows for the use of nonpolar solvents. Of the nonpolar solvents tested, n-dodecane was found to have superior selectivity and conversion at room temperature, as shown in Table 1.1.[2]

Solvent	Rxn. P (bar)	Convers. (%)	Select. (%)
Methanol	27	35	>99
THF	27	20	>99
Ethyl acetate	27	48	86
Water	25	<5	>99
Acetic acid (glacial)	22	>99	84
Acetic acid (aq, pH=4.7)	24	20	>99
Dodecane	23	>99	>99

Table 1.1: Solvent exploration for catalytic HDO of benzyl alcohol

The Vannucci group proposed a reaction pathway (Figure 1.2) based on kinetic studies; however, the intermediate in this pathway has not yet been identified. Two possible intermediates were proposed, each with their own corresponding pathway. The first pathway (Figure 1.3) involves the reduction of the $Pd^{(II)}$ center to the $Pd^{(0)}$ oxidation state,

followed by benzyl C-O bond cleavage and subsequent protonation to yield the final products and the re-oxidized $Pd^{(II)}$ complex. The second pathway (Figure 1.4) consists of the formation of a Pd hydride species, which in turn displaces the hydroxyl group from the benzyl carbon to produce toluene. The complex is then deprotonated by the hydroxyl group, forming water and regenerating the catalyst complex. However, the intermediate geometry, which would allow for identification of which pathway corresponds to this reaction, has not been determined experimentally.

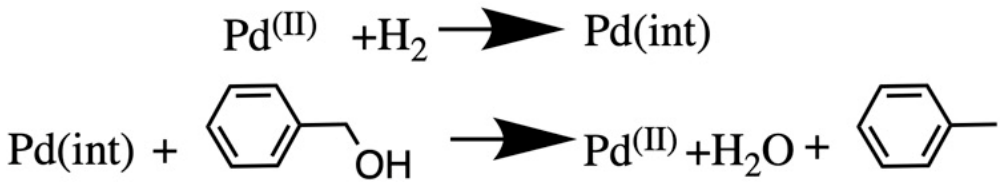

Figure 1.2 General reaction pathway proposed by Delucia *et al*[1]

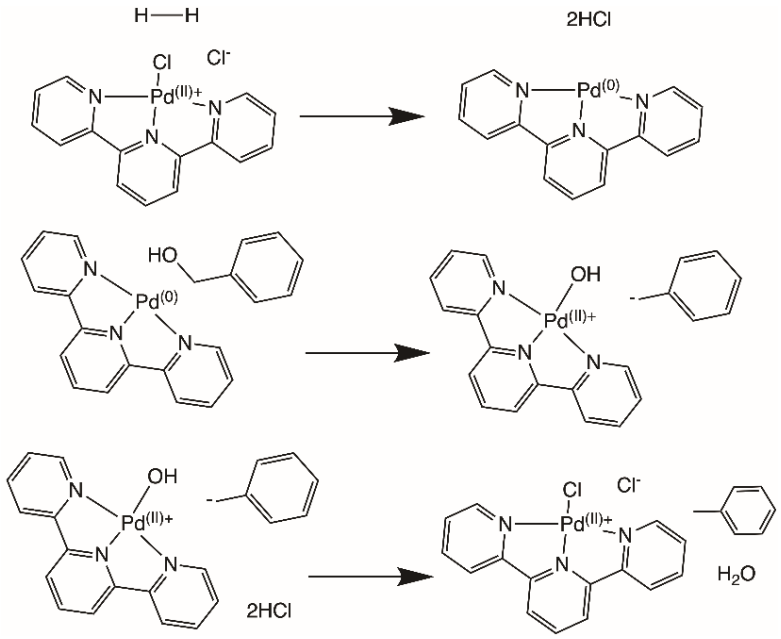

Figure 1.3: Reductive intermediate pathway[2]

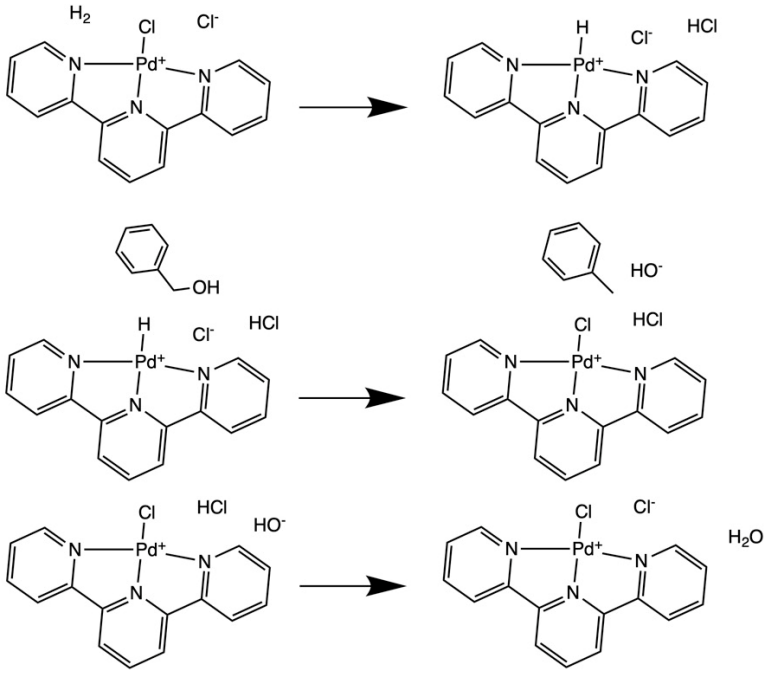

Figure 1.4: Hydride intermediate pathway[1,2]

To gain molecular level insight on these reactions, computer simulations are needed. These simulations allow us to explore the interaction between the catalyst complex and the amorphous silica surface to which it is bound, leading to determination of the catalyst complex geometry at each step of the HDO reaction pathway. DFT calculations[2,6] suggest the catalyst binds to the silica surface either through Coulombic interactions or covalent bonding with a deprotonated carboxyl linkage (Figure 1.5). Regardless of the binding method, it is believed that the complex lies parallel to the silica surface[7] as shown in Figure 1.6. This project, however, focuses on the geometries of the catalyst intermediate during the HDO reaction. To that end, we do not consider the silica surface in this project for the sake of computational expense.

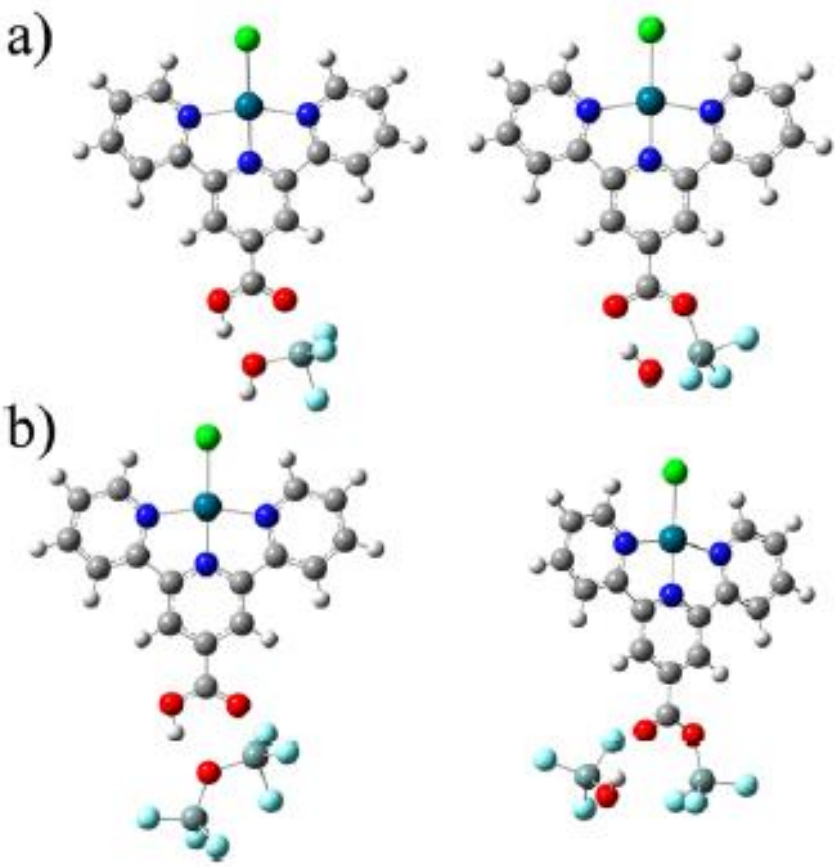

Figure 1.5: Pdtpy catalyst bound to amorphous silica surface at (a) silanol sites and (b) siloxane sites[2,6]

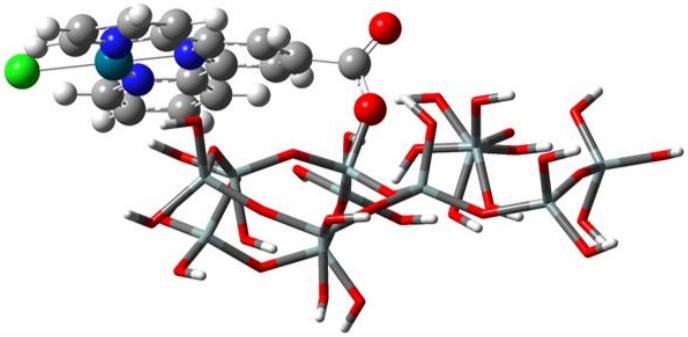

Figure 1.6: Pdtpy complex parallel to amorphous silica surface[7]

We present an overview of the existing research in this field in Chapter 2. After this, we describe the computational methods used in Chapter 3. Next, we present the results of

our calculations for the reductive and hydride pathways proposed by our collaborators in Chapter 4. After that, we provide a comparison of the reaction pathway energies and geometries to determine which reaction pathway is energetically favored in Chapter 5. Finally, we present a summary of our conclusions in Chapter 6.

Chapter 2: Literature Review

Lignin, an inedible polymer component of biomass, is being investigated as a potential source of biofuels and other organic compounds. In industrial settings, lignin is frequently treated as a waste product, as cellulose is favored for purposes of biofuel production and the production of paper products.[8–10] The principal issue with the usability of lignin as a biofuel feedstock is its high oxygen content,[10–12] which leads to chemical and thermal instability[10], some corrosive properties[12], and under certain conditions, the formation of undesirable coke-like byproducts.[11] One solution is to remove as much oxygen as possible. This is typically accomplished through a process called hydrodeoxygenation (HDO), where oxygen is replaced with hydrogen, producing either water or an alcohol as a by-product.[10]

Bio-oils derived from lignin are produced by depolymerization, most commonly through pyrolysis.[1,10–13] These bio-oils frequently have many components, including phenyl and benzyl alcohols, esters, ketones, and aldehydes. Rather than conducting studies on the many compounds present in lignin-derived bio-oils, model compounds are used to design catalysts for HDO. These are later generalized for use with other compounds that occur in bio-oil. Several studies have shown that molecular catalysts with transition metal centers have increased selectivity towards HDO with preservation of aromaticity.[1,2,14,15]

The most common model lignin compounds are phenyl alcohols and phenyl ethers, including guaiacol[10,16–23] and anisole (Figure 2.1).[13,20] For both of these compounds, the activation of H_2 has been shown to be a key step in the reaction pathway.[20] Additionally, it is important to use a catalyst that avoids over-hydrogenation to form cyclohexane. Guaiacol tends to react by demethylation-HDO to produce phenol,[10,16] followed by subsequent hydrogenation to produce cyclohexane. Similarly, anisole tends to react either by demethylation-HDO to produce benzene or by transalkylation-HDO to produce toluene. There are also nickel and iron-based catalysts[13,20] that show selectivity to produce both benzene and toluene from both guaiacol and anisole.

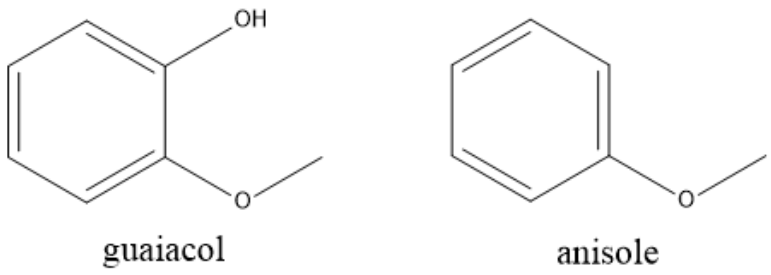

Figure 2.1: Guaiacol and anisole, two common model lignin monomers

HDO reactions are catalyzed by noble metals,[12,16,17] metal-doped surfaces,[2,14] transition metal sulfides,[12] or transition metal molecular catalysts.[1,2,14] However, many of these catalysts do not have the selectivity to preserve the aromaticity of the monomers present in lignin,[2,10,24] a desirable characteristic due to the increased energy density[2,12] and stability of these aromatic compounds, as well as their utility in other contexts as reagents or solvents.

Research on HDO has focused on silica,[2,25] alumina,[18,26–28] or zirconia[18]-supported metal catalysts and on molecular catalysts.[1,2,14,15] Supported metal catalysts and pure metals

are widely used for their simplicity, as they do not require elaborate synthetic procedures. Molecular catalysts with highly coordinated metal centers have been researched as an improvement to these, as they provide increased selectivity towards deoxygenation without ring hydrogenation.[1,29,30] This is an important quality for biofuel upgrading, as preserving the aromaticity of the fuel increases its aromaticity relative to the fully hydrogenated products common in reactions with lesser selectivity.[10,13]

Chapter 3: Methods

3.1: Hartree-Fock Method

Quantum chemistry calculations require solving the electronic Schrödinger equation. However, it is not possible to analytically determine a wavefunction for a multi-electronic system,[31] and computational chemists must use approximate methods. The most basic of these approximate methods is the Hartree-Fock (HF) method, which uses a single Slater determinant. A Slater determinant is an anti-symmetrized product of orthogonal one-electron wavefunctions called spin orbitals. The energy of the system is calculated using the HF equation (eq. 3.1.1)[31,32]

$$\boldsymbol{FC} = \boldsymbol{SC\epsilon} \qquad \text{(eq. 3.1.1)}$$

$$\hat{f}(1) = \hat{h}(1) + \sum_b \hat{J}_b(1) - \hat{K}_b(1) \qquad \text{(eq. 3.1.2)}$$

$$\hat{h}(i) = \frac{-1}{2}\nabla_i^2 - \sum_{A=1}^{M} \frac{Z_A}{r_{iA}} \qquad \text{(eq. 3.1.3)}$$

$$\hat{J}_b(i)\chi_a(i) = \int d\boldsymbol{x}_j \frac{|\chi_b(j)|^2}{r_{ij}}\chi_a(i) \qquad \text{(eq. 3.1.4)}$$

$$\hat{K}_b(i)\chi_a(i) = \int d\boldsymbol{x}_j \frac{\chi_b^*(j)\chi_a(j)}{r_{ij}}\chi_b(i) \qquad \text{(eq. 3.1.5)}$$

Where $\boldsymbol{F}$ is the Fock matrix, $\boldsymbol{S}$ is the overlap matrix, $\mathbf{C}$ is a vector of the coefficients for each orbital, and $\boldsymbol{\epsilon}$ is a diagonal matrix of orbital energies. The elements of $\boldsymbol{F}$ are given by $F_{\alpha\beta} = \langle\chi_\alpha|\hat{f}|\chi_\beta\rangle$, and the elements of $\boldsymbol{S}$ are given by $S_{\alpha\beta} = \langle\chi_\alpha|\chi_\beta\rangle$. The Fock operator $\hat{f}$ (eq. 3.1.2) is the sum of the one-electron Hamiltonian (eq. 3.1.3), the Coulomb operator ($\hat{\mathrm{J}}$, eq. 3.1.4), and the exchange operator ($\hat{K}$, eq. 3.1.5). The operator $\hat{\mathrm{J}}$ represents the Coulombic interaction between two electrons. The operator $\hat{K}$, which has no classical analogue, arises from the antisymmetry of the wavefunction with respect to an exchange of electron indices.

The functions used to construct the Slater determinants are defined by a basis set, consisting of atomic functions. For this work, these atomic functions are made up of Gaussian functions called primitives.[32] These Gaussian functions are of the form:

$$g_p(\zeta, r) = nx^a y^b z^c e^{-\zeta \boldsymbol{r}^2} \qquad \text{(eq. 3.1.6)}$$

A linear combination of primitives is used to generate the atomic orbital basis functions χ used in the HF equation.[32] The exponents *a*, *b*, and *c*, along with the *x*, *y*, and *z* terms in the primitive control the shape of each orbital. The exponents sum to the angular momentum quantum number *l*. The *n* term serves as a normalization constant, ensuring that the integral over all space of the function squared is equal to 1 (a necessary property for a probability distribution). The ζ term in the exponential controls the diffuseness or tightness of the primitive. Modification of the basis set specification changes how many primitives are used

for the basis functions of each atom and what type of primitive is used in each. For larger atoms, such as heavy metals, the number of core electron basis functions can make computations cost-prohibitive. Since core electrons do not directly participate in interatomic interactions, we can treat them with an effective core potential,[33] which mimics the shielding behavior of the core electrons rather than explicitly calculating their effects.

3.2: Density Functional Theory (DFT)

All energy calculations were conducted using DFT. Kohn-Sham (KS) DFT is based on the HF method, but solves for the energy of the system using a functional of the electron density instead of the wavefunction of the system.[34,35] This is possible under the first Hohenberg-Kohn theorem,[34] which states that the external potential for a system is a unique functional of the ground state electron density. The second Hohenberg-Kohn theorem states that the correct ground state electron density for the system can be used to determine the ground state energy by the variational method.[34] These two theorems are the foundation for DFT, and using this method we can determine the ground state energy for a system with higher accuracy than HF, [34,36] because HF does not include a full treatment of electron correlation,[32] an effect that KS-DFT methods include by using an exchange-correlation energy functional.[37,38]

3.3: Dispersion

Dispersion is an attractive interaction of the van der Waals (vdW) type between molecules with negligible electron density overlap.[36,39] It is caused by induced dipoles between non-covalently bonded particles and are an attractive force, although with a smaller

magnitude than other noncovalent interactions like hydrogen bonds and dipole-dipole interactions.[35,36,39–41] Dispersion interactions are more costly to compute accurately with standard KS-DFT in comparison with covalent interactions, as vdW-type interactions have a relatively flat potential energy surface (PES)[40] in comparison to interactions with higher electron density overlap. Because dispersion interactions play a major role in reactions involving nonpolar solvents and aromatic compounds,[35,40] it is vital to use a method that will accurately calculate the effects of dispersion. Many such methods exist, including Møller-Plesset perturbation theory (MP), coupled-cluster theory (CC), or dispersion-corrected density functionals.[36,38,40] In this project, we use the dispersion-corrected density functional ωB97X-D,[36,38,42] as this is more computationally affordable than using MP or CC while still accurately accounting for the effects of dispersion.

3.4: Solvation Methods

Calculations in solution were performed using the Solvation Model based on Density (SMD) method.[6,43] SMD uses the quantum mechanical charge density of solute molecules while describing the solvent as a dielectric medium with surface tension at the solute cavity boundary, effectively creating a bubble within the solvent in which the solute is contained. SMD differs from other continuum models by calculating both bulk electrostatic and non-bulk-electrostatic terms. Because the free energy of solvation is a state function, there are several thermodynamically-valid ways of dividing the bulk electrostatic and non-bulk-electrostatic terms.[43] The electrostatic term is generated by the integral-equation-formalism polarizable continuum model (IEF-PCM[44–46]) method, an improvement on the standard PCM procedure that accounts for isotropic and intrinsically anisotropic solvents, as well as ionic

solutions. The non-bulk-electrostatic term for the SMD method arises from dispersion interaction between the solute and the solvent molecules in the first solvation shell and is not considered in the bare IEF-PCM method. The final free energy is given by:

$$\Delta G_S^o = \Delta G_{ENP} + \Delta G_{CDS} + \Delta G_{conc}^o \quad \text{(eq. 3.4.1)}$$

The free energy of solvation is written as the sum of the solute electronic, nuclear, and polarization components (ENP), the solvent cavitation, dispersion, and structure components (CDS), plus a term to account for the concentration (conc) change between gas and liquid phase standard states for the solution. The ENP term is the difference in electronic, nuclear, and polarization free energies between the gas-phase structure and the liquid-phase structure without any solvent correction. If the gas and liquid phase geometries are the same, the ENP term becomes an electronic polarization term as the nuclear term goes to zero. The CDS term is determined based on the solvent-accessible surface area of each atom, the atomic surface tension, and the molecular surface tension. These are calculated by:

$$G_{CDS} = \sum_k^{atoms} \sigma_k A_k\left(\boldsymbol{R}_{\boldsymbol{Z_k}}, \{R_{Z_k} + r_s\}\right) + \sigma^{[M]} \sum_k^{atoms} A_k\left(\boldsymbol{R}_{\boldsymbol{Z_k}}, \{R_{Z_k} + r_s\}\right) \quad \text{(eq. 3.4.2)}$$

Where σ_k and $\sigma^{[M]}$ are the atom k and molecular surface tension, respectively, A_K is the solvent accessible surface area of atom k, $\boldsymbol{R}$ is the set of atomic vdW radii, and r_s is added to the vdW radius to determine the solvent accessible surface area.[43]

The surface tensions discussed throughout this section are a semiempirical term that accounts for short-range non-bulk electrostatic interactions and nonelectrostatic effects like dispersion, solvent structural effects, and cavitation. The inclusion of these effects gives an

improvement in certainty of cavity definition from prior methods developed by Marenich and coworkers.[43]

3.5: Geometry Optimization Methods

Geometry optimizations find the stationary point on a potential energy surface (PES). In this project, geometry optimizations are conducted using the Berny optimization algorithm. This algorithm, originally proposed by H. Bernhard Schlegel,[47] is a modified conjugate gradient algorithm to optimize the molecular geometry. The key difference between Schlegel's algorithm and other conjugate gradient algorithms is that this algorithm uses the Hessian matrix, a matrix of all mixed partial derivatives of the PES with respect to the Cartesian coordinates of each nucleus, rather than its inverse. This decreases the computational cost of the optimization. First, the initial geometry guess is given and the energy, gradient vector, and Hessian matrix are calculated. Next, an orthonormal set of vectors is constructed for the space. This set is spanned by vectors generated by the displacement of each point from the previous point. Using these vectors, the second derivatives are estimated, and are then used to update the estimated second derivative matrix $\boldsymbol{F}$. The matrix $\boldsymbol{F}$ is an approximation of the Hessian, and is less computationally expensive to update at each step than recalculation of the Hessian. After the second derivative matrix is updated, a search for a minimum energy along each basis vector is done by fitting a quartic polynomial between the current and previous energies and gradients. The gradients at this point are interpolated from the current and previous energies. These gradients are then used with the estimated second derivative matrix to determine the next stationary point.

After each optimization step, the gradient and displacement vectors are tested for convergence, where the root-mean-square (RMS) gradient, absolute value of the largest gradient component, RMS displacement, and largest displacement vector component must fall below convergence thresholds defined for the specific optimization. The optimization procedure repeats until a predetermined maximum number of steps or the optimization conditions are all met.

Transition-state geometries are also obtained using the Berny optimization algorithm[47] with a modification forcing the second derivative matrix to include exactly one negative eigenvalue. This requires that the starting geometry guess is close to an appropriate transition state geometry. The negative eigenvalue of the second derivative matrix corresponds to a vibrational mode in which the frequency is imaginary. Within the harmonic oscillator approximation, the vibrational frequency of a normal mode is proportional to the square root of the force constant. The force constants for the vibrational modes of a system are the eigenvalues of the Hessian, which is approximated in the Berny algorithm by the approximate second derivative matrix $\boldsymbol{F}$. This vibrational mode corresponds to the lowest energy pathway between the reactant and product minima locations on the PES. The geometry of the transition state corresponds to a saddle point on the PES, in which there is a local maximum in one dimension and a local minimum in all others. By imposing the requirement that the second derivative matrix includes exactly one negative eigenvalue, the saddle point is reached and the transition state geometry is determined.

3.6: Intrinsic Reaction Coordinate

An intrinsic reaction coordinate (IRC)[48] is the minimum energy pathway between two minima that passes through the transition state. Mathematically, the IRC is determined by finding the solution to the set of simultaneous equations:

$$\frac{dx_1}{\frac{\partial V}{\partial x_1}} = \frac{dx_2}{\frac{\partial V}{\partial x_2}} = \cdots = \frac{dx_{3n}}{\frac{\partial V}{\partial x_{3n}}} \qquad \text{(eq. 3.6.1)}$$

Where V refers to the potential energy function of the system, the subscript n refers to the number of nuclei and x_i refers to the mass-weighted Cartesian coordinates for each nucleus, given by eq 3.6.2

$$M_\alpha^{1/2} X_\alpha = x_{3\alpha-2}, M_\alpha^{1/2} Y_\alpha = x_{3\alpha-1}, M_\alpha^{1/2} Z_\alpha = x_{3\alpha} \qquad \text{(eq. 3.6.2)}$$

Where X_α, Y_α, and Z_α are the Cartesian coordinates of nucleus α and M_α is the mass of nucleus α. The solution of eq 3.6.1 determines the "center line", or lowest energy pathway between two minima on the reaction's PES. However, this method is computationally expensive in comparison to a single geometry optimization.

We use an approximation of the IRC to confirm the transition states calculated using the Berny optimization algorithm discussed in section 3.5. First, the normal mode corresponding to the negative eigenvector of the second derivative matrix described in section 3.5 is found, and the transition state geometry is distorted along this normal mode in each direction. The distorted transition state geometries are optimized, yielding minima in each direction that correspond to the reactant and product geometries associated to this transition state. This significantly less expensive procedure allows for us to confirm the

validity of a transition state without calculating an IRC. However, this method has the risk of missing a closer local minimum, which does not happen in the IRC method. We implement this procedure with our initial transition state guess at a low level of theory (in our case, B3LYP[49,50]/3-21G with Grimme's D3[51] dispersion model and without solvent corrections) to quickly and inexpensively screen any guesses that do not correspond to the correct reactant and product minima. After this, we take the successful transition state guesses and re-optimize them at a higher level of theory and determine the IRC at that point.

3.7: Computational Details

All computations were conducted with a development version of the Gaussian[52] computational chemistry software suite. For all reported results, we used the ωB97X-D[38,42] functional discussed above. We treat the Pd center with the Def2TZVP basis set and Stuttgart's pseudopotentials,[33] and all other centers with the 6-31++G(2d,p) basis set. Def2TZVP is used for Pd because it has high accuracy for this element[6,53,54], and 6-31++G(2d,p) is used for all other centers due to its high accuracy for long-range effects, such as hydrogen bonds, π-π stacking, and dispersion interactions. Stuttgart's pseudopotentials are implemented for the Pd center as described in section 3.1 to decrease computational cost. Solvation is modeled using the SMD method discussed in section 3.4: with n-dodecane as the solvent.

DFT is used for this work because of its high accuracy at a relatively low cost compared to other methods. Dispersion-corrected DFT very accurately models experimentally-observed trends[35,36,38–40] at a much lower computational cost than other methods discussed in section 3.3: The use of the dispersion-corrected functional ωB97X-D,

along with treating the Pd center with effective core potentials, allow us to reduce the computational cost of our calculations while still achieving a reliable result.

All structures presented in this project are generated using the GaussView chemical modeling program and are modeled in solvent, though they do not change significantly between solvent and gas-phase calculations. These geometries were then optimized using the Berny optimization algorithm discussed in section 3.5: . Transition state geometries were then verified according to the imaginary normal mode displacement algorithm discussed in section 3.6 and by IRC calculation.

Chapter 4: Results

The hydrodeoxygenation of benzyl alcohol (BA) to toluene (tol) with the Pdtpy catalyst complex proceeds by the mechanism in Figure 1.2.[2] However, the structure of the intermediate cannot be determined experimentally. The Vannucci group has proposed two intermediates, whose corresponding mechanisms are shown in Figure 1.3 and Figure 1.4. The first intermediate proposed is a reduced Pd compound (Figure 1.3), which catalyzes the cleavage of the benzyl C-O bond to produce a tpyPd-OH species and a benzyl carbanion, both of which are protonated. The second intermediate is a Pd-hydride species (Figure 1.4), which then protonates the benzyl carbon and yields a hydroxyl anion to be protonated. In our simulations, we also found a third possible pathway in which the terpyridine system is opened before a hydride is formed, then reacting similarly to the closed hydride pathway. In order to determine which of these pathways is more energetically favored, we performed DFT calculations for each pathway.

There are some steps in each reaction pathway that were not considered for this work: 1) After the rate-determining step for each of the hydride pathways discussed, there is a hydroxide species that is protonated; 2) after the rate-determining step for the reductive pathway, there is a $Pd^{(II)}$-OH intermediate and a toluene carbanion intermediate that are both protonated to yield the final products. These steps are not discussed here because they are not rate-determining, as the ionic species are significantly less stable in a nonpolar environment than the neutral species formed as a result of these protonation steps.

4.1: Reductive Pathway

The reductive pathway proceeds in 3 steps, as shown in Figure 1.3. The relevant structures for this pathway are given in Figure 4.2, and the energies are shown in Figure 4.1. In this pathway, the palladium center is reduced from the +2 to the 0 oxidation state, and the catalyst complex adopts a puckered configuration (Figure 4.2a). This reduction step is accompanied by a relative energy increase of 46.19 kcal/mol in the gas phase and 56.97 kcal/mol in n-dodecane. After the complex is reduced, the BA substrate approaches the complex, stabilizing the overall complex by 14.62 kcal/mol in the gas phase and by 9.99 kcal/mol in n-dodecane. When the BA substrate nears the complex, the $Pd^{(0)}$ center facilitates the cleavage of the benzyl C-O bond (Figure 4.2c), forming a secondary tpy$Pd^{(II)}$-OH intermediate and releasing a benzyl carbanion as a result. The RDS transition state is higher in energy than the intermediate by 45.89 kcal/mol in the gas phase and by 33.38 kcal/mol in n-dodecane, but the benzyl carbanion product and remaining Pd-hydroxy intermediate are then protonated, yielding the final products of tol and water, accompanied by a relative energy decrease of 62.73 kcal/mol in the gas phase and 86.39 kcal/mol in n-dodecane. The

energy profile for this pathway is shown in Figure 4.1, and each reaction step is summarized in Table 4.1, along with several key geometric parameters.

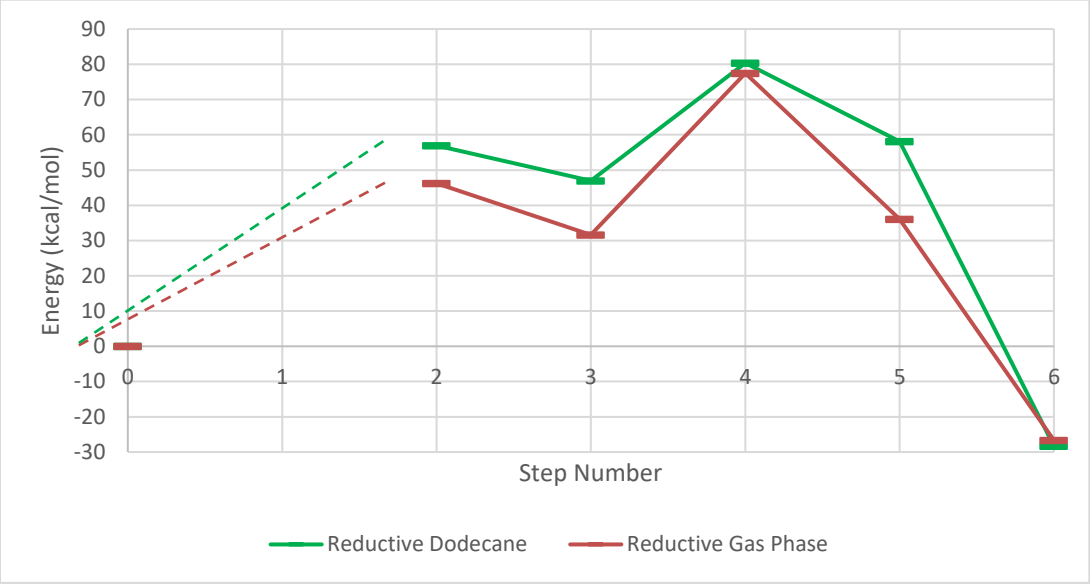

Figure 4.1: Reductive pathway energy profile

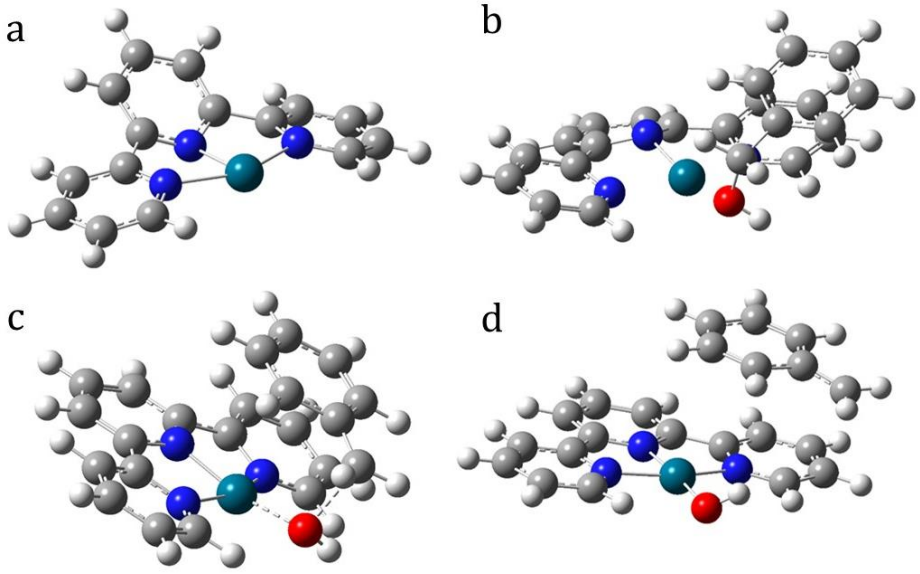

Figure 4.2: Reductive pathway key geometries, a) Pd(0) intermediate, b) the reduced catalyst with benzyl alcohol, c) reductive pathway rate-determining step transition state, and d) Pdtpy-OH intermediate with toluene carbanion

Step #	Description	R(N,Pd) (Å)	R(N',Pd) (Å)	R(N'',Pd) (Å)	R(Pd,N) average (Å)	A(N',Pd,4'C) (degrees)	Pd Mulliken charge (au)	Average py-py distance (Å)
0	Initial catalyst (Fig.	1.95	2.05	2.04	2.01	161.3	1.1	1.48
2	Reduced intermediate	2.21	2.19	2.19	2.20	152.3	0.1	1.48
3	Pd(0) complex with BA	2.05	2.17	2.16	2.12	153.9	0.2	1.46
4	RDS TS	1.94	2.05	2.07	2.02	158.5	0.6	1.45
5	tpyPd-OH + tol·	1.95	2.03	2.04	2.01	161.5	0.8	1.47
6	Final products	1.95	2.05	2.04	2.01	161.3	1.1	1.48

Table 4.1: Key geometric parameters for the reductive pathway. Atom shorthand given in Figure 4.3

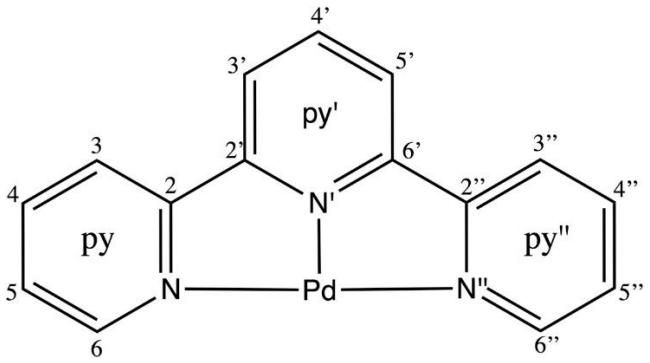

Figure 4.3: Key for atom labelling for Table 4.1

As shown in Table 4.1 and in Figure 4.2, there is a noticeable (9.1°) decrease in the Pd-N'-4'C angle over the course of the reaction pathway. This occurs as the localized charge on the Pd center changes, indicated by the Mulliken charge on the Pd center here. We also see fluctuations of up to 0.26Å in each of the three Pd-N bonds as the reaction progresses. However, we can also note that the distance between the pyridine rings, defined by the bond lengths between 2C-2'C and 6'C-2''C, is nearly constant over the course of the reaction.

4.2: Hydride Pathway

The hydride pathway also consists of three steps (Figure 1.4). In the first reaction, the hydride is formed (closed in Figure 4.4, open in Figure 4.5), releasing as a byproduct one molecule of HCl. After the hydride forms, it then attacks the benzyl carbon, displacing the hydroxyl group, which is then protonated by the remaining HCl in solution. As stated earlier, a second possible hydride intermediate pathway was found. The first of these proceeds with the catalyst complex remaining closed (referred to as the "closed pathway"), while the second has the additional prior step of the terpyridine ring system opening (referred to as the "open pathway")

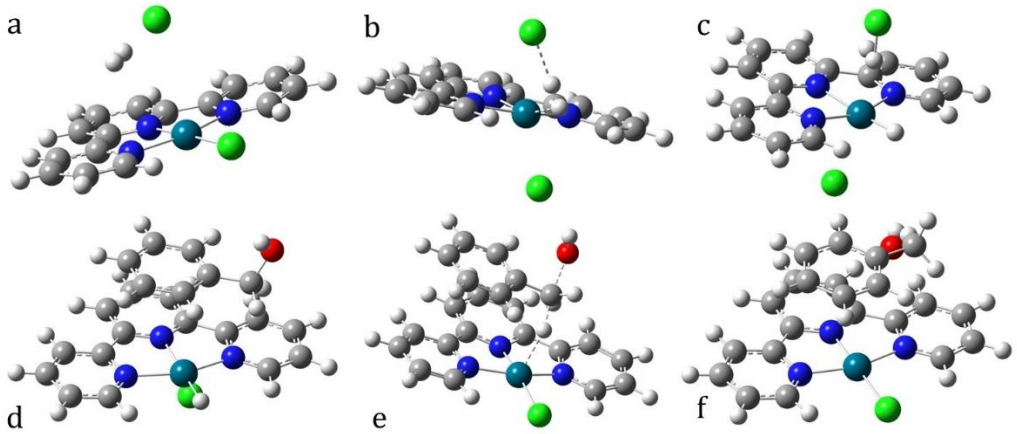

Figure 4.4: Closed hydride pathway geometries, a) catalyst with H_2, b) hydride formation transition, c) hydride intermediate formed with remaining HCl, d) hydride intermediate with benzyl alcohol, e) rate-determining step transition state, and f) catalyst returning to original structure

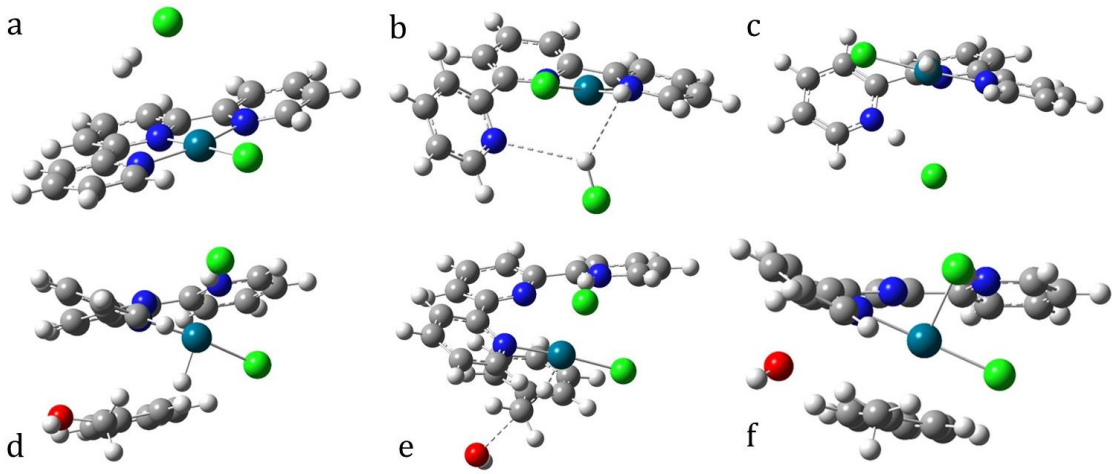

Figure 4.5: Open hydride pathway geometries, a) catalyst with H_2, b) hydride formation transition state, c) hydride intermediate formed with remaining Cl^-, d) hydride intermediate with benzyl alcohol, e) rate-determining step transition state, and f) catalyst returning to original structure

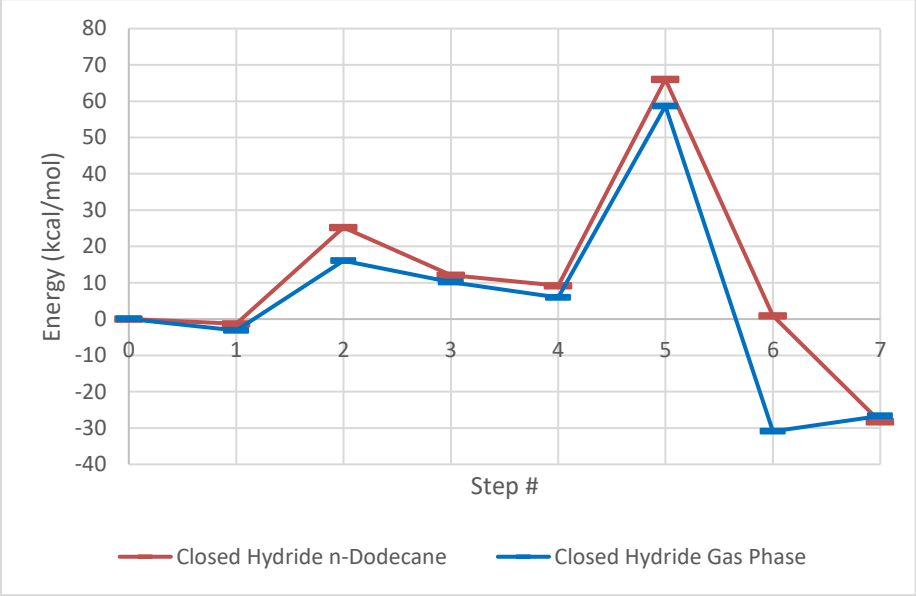

Figure 4.6: Energy profile of the closed hydride pathway

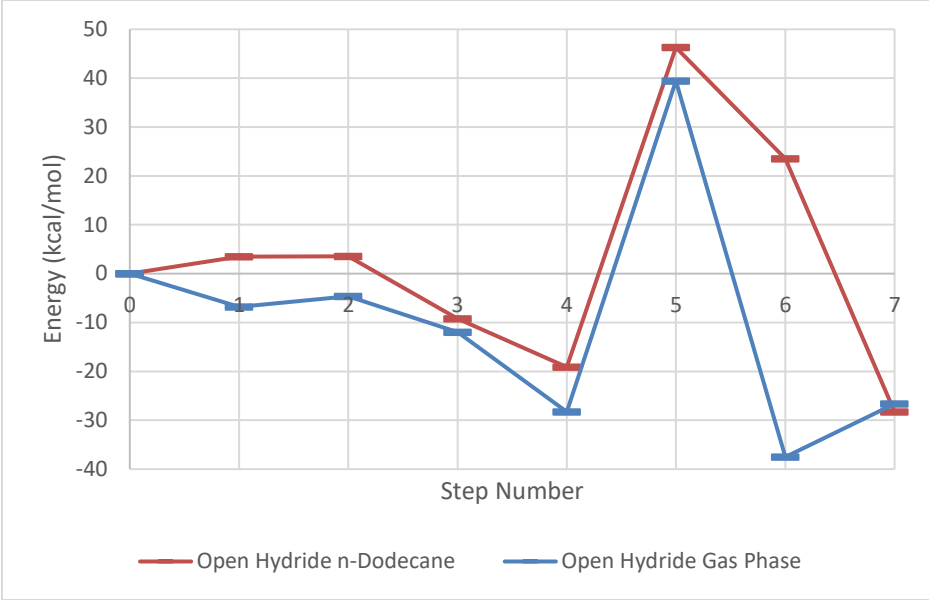

Figure 4.7: Energy profile of the open hydride pathway

4.2.1: Closed Hydride Pathway

The closed hydride pathway proceeds with the hydride forming from the closed catalyst in its original square planar geometry (Figure 4.4a), requiring an activation energy of 16.10 kcal/mol in the gas phase and 25.27 kcal/mol in n-dodecane. The resulting hydride has a relative energy increase of 10.14 kcal/mol in the gas phase and 12.12 kcal/mol in n-dodecane, compared to the initial reactants. After the hydride forms, the reaction then proceeds, yielding the original complex as the toluene and water products are formed with an activation energy of 58.66 kcal/mol in the gas phase and 56.86 kcal/mol in n-dodecane relative to the hydride intermediate. The RDS is exothermic by 36.88 kcal/mol in the gas phase and 8.26 kcal/mol in n-dodecane relative to the intermediate. The energetics of this pathway are shown in Figure 4.6 and are reported in Table 4.3.

4.2.2: Open Hydride Pathway

In the open hydride pathway, the terpyridine system opens by breaking the bonds between two of the three nitrogen centers and the Pd center, yielding a net energy decrease of 6.80 kcal/mol in the gas phase and an increase of 3.50 kcal/mol in n-dodecane. After this, the reaction proceeds to the formation of the hydride intermediate with an activation energy of 2.18 kcal/mol in the gas phase and 0.03 kcal/mol in n-dodecane. The HCl that results from the initial hydride formation step protonates the nitrogen that is no longer bound to the Pd center, yielding a hydride intermediate species that is 11.94 kcal/mol lower in energy than the initial reactants for the gas phase and 9.19 kcal/mol lower in n-dodecane. The open hydride complex then proceeds through the HDO reaction as described above in Figure 1.3, and the new pyridyl N-H bond protonates the hydroxyl group that is displaced from the benzyl carbon as the terpyridine system reforms around the Pd center as seen in figure 4.2.2a, with an activation energy of 67.73 kcal/mol relative to the hydride intermediate in the gas phase and 65.42 kcal/mol in n-dodecane. The products of the RDS for this pathway are lower in energy by 9.23 kcal/mol relative to the hydride intermediate in the gas phase, but higher in energy by 42.67 kcal/mol in n-dodecane. Once the hydroxyl group is protonated, the final product is 26.66 kcal/mol lower than the initial reactants in the gas phase and 28.29 kcal/mol lower in n-dodecane. The energetics of this pathway are shown in Figure 4.7 and are reported in Table 4.3.

4.2.3: Comparison of Hydride Pathways

The key difference between the two hydride pathways lies in the complex structure. As shown in Figure 4.8, the change in energy between the open and closed hydride pathways is a relative stabilization of the hydride intermediate by 21.31 kcal/mol. However, as given by the imaginary normal mode corresponding to the two RDS transition states, the interaction between the Pd-H and the benzyl carbon are extremely similar (Figure 4.4e, Figure 4.5e), so it is likely that the energy difference for this pathway is mostly due to the stabilization of the hydride intermediate species.

The open hydride pathway is more favorable than the closed hydride pathway relative to the initial reactants. However, compared to the intermediate geometry, the RDS activation energy is 1.57 kcal/mol lower in the closed hydride pathway than for the open. This is due to the stabilization of the hydride intermediate. While the overall reaction energy compared to the initial reactants is lower in the open hydride, the intermediate geometry is 9.19 kcal/mol lower in energy than the reactants, compared to the closed hydride intermediate energy of 12.12 kcal/mol higher than the reactants. Because of this, it is preferable to refer to the activation energy as the difference between the RDS TS (point 5 in Figure 4.8) and the intermediate (point 4 in the same figure).

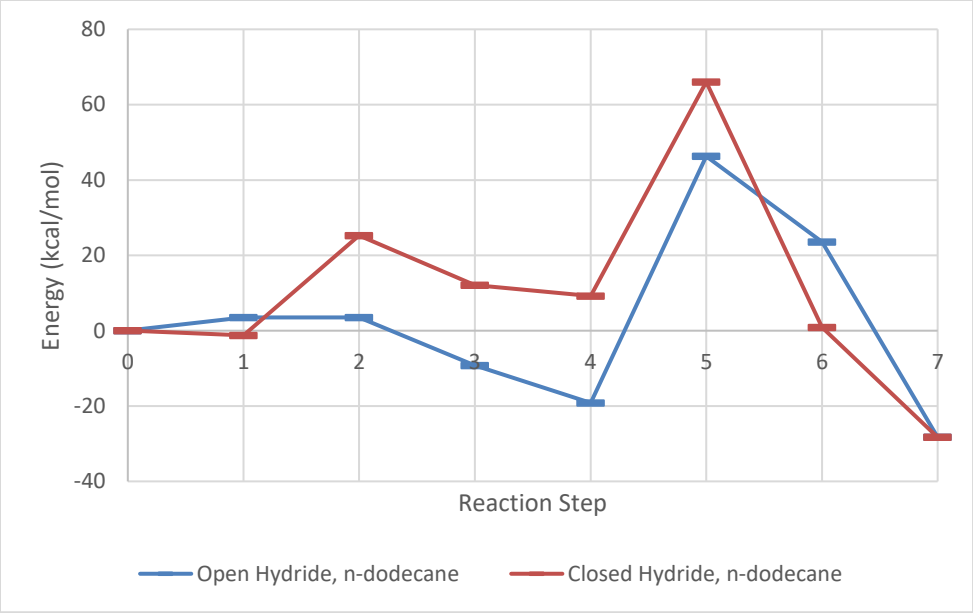

Figure 4.8: Comparison of open and closed hydride pathway energies

4.3: Comparison of All Pathways

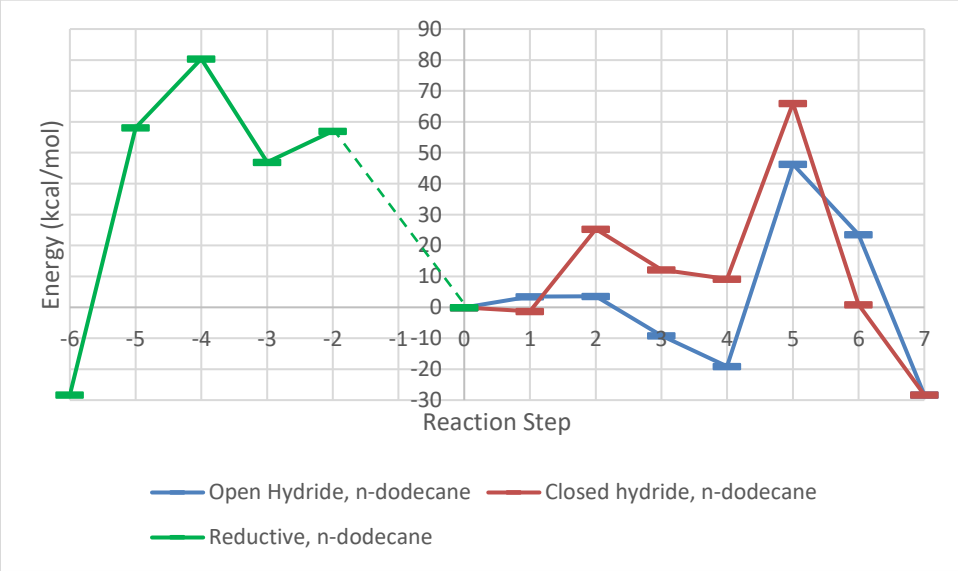

Figure 4.9: Comparison of all pathways

The geometries and corresponding energies considered in Figure 4.9 are reported in Table 4.2 and Table 4.3. As we can see in Figure 4.9, the reductive pathway has a significantly

higher activation energy (80.36 kcal/mol in n-dodecane) than the open hydride pathway (46.29 kcal/mol in n-dodecane) or the closed hydride pathway (66.03 kcal/mol in n-dodecane). However, as discussed in section 4.2.3: the activation energy for the intermediate formation should be considered in addition to the overall energy difference between the RDS TS and the reactants. Keeping this in mind, we see that the intermediate formation is more favored for the open hydride (-9.19 kcal/mol) than for the closed hydride (+12.12 kcal/mol) or the reductive intermediate (56.97 kcal/mol).

While the open hydride pathway has a lower overall energy (46.29 kcal/mol relative to reactants) than the closed hydride pathway (66.03 kcal/mol relative to reactants), the relative stability of the open hydride intermediate compared to the closed hydride could have a major impact on which pathway is truly favored. Because these two intermediates can interconvert, there will exist an equilibrium between the two. The overall barrier for the closed hydride to react by the closed pathway is higher than the barrier for conversion to the open hydride pathway, meaning that the open hydride pathway would be favored.

Step Number	Corresponding Geometry	Relative Energy (kcal/mol)
0	Zero of energy, all reactants at infinite distance	0
-2	Reduced intermediate, fig. 4.1.2a	56.97
-3	Reduced catalyst with benzyl alcohol, fig. 4.1.2b	46.98
-4	Rate-determining step transition state, fig. 4.1.2c	80.36
-5	Pdtpy-OH intermediate with toluene carbanion, fig. 4.1.2d	58.10
-6	Final products at infinite distance	-28.29

Table 4.2: Reductive pathway reaction steps and their corresponding geometries

Step Number	Corresponding Geometry	Relative energy for closed hydride (kcal/mol)	Relative energy for open hydride (kcal/mol)
0	Zero of energy, all reactants at infinite distance	0	0
1	Catalyst with H_2, fig. 4.3.4	-1.24	3.50
2	Hydride formation transition state, fig. 4.3.1 (closed)/4.3.2 (open)	25.27	3.54
3	Hydride intermediate formed with HCl, fig. 4.3.7 (closed)/4.3.8 (open)	12.12	-9.19
4	Hydride intermediate with benzyl alcohol, fig. 4.3.9 (closed)/4.3.10 (open)	9.18	-19.13
5	Rate-determining step transition state, fig. 3.3.1 (closed)/3.3.2 (open)	66.03	46.29
6	Catalyst returns to original structure, fig. 4.3.11 (closed)/4.3.12 (open)	0.91	23.54
7	Final products at infinite distance	-28.29	-28.29

Table 4.3: Hydride reaction pathway steps and their corresponding geometries

Chapter 5: Discussion

5.1: Reductive Pathway

In the reductive pathway, the complex adopts a puckered geometry as the Pd center is reduced. Upon investigating the geometries for the pathway, we can see that this is explained by the relative invariance of the bond lengths between pyridine groups as the reaction progresses (Figure 5.1) while the Pd-N bond distances all vary noticeably (

Figure 5.2) due to the changes in charge density as the reaction progresses (Figure 5.3), but the C-C bonds that connect the pyridines remain fairly constant over the course of the

reaction. Due to these constraints, the complex is deformed into the puckered conformation we observe (Figure 5.4).

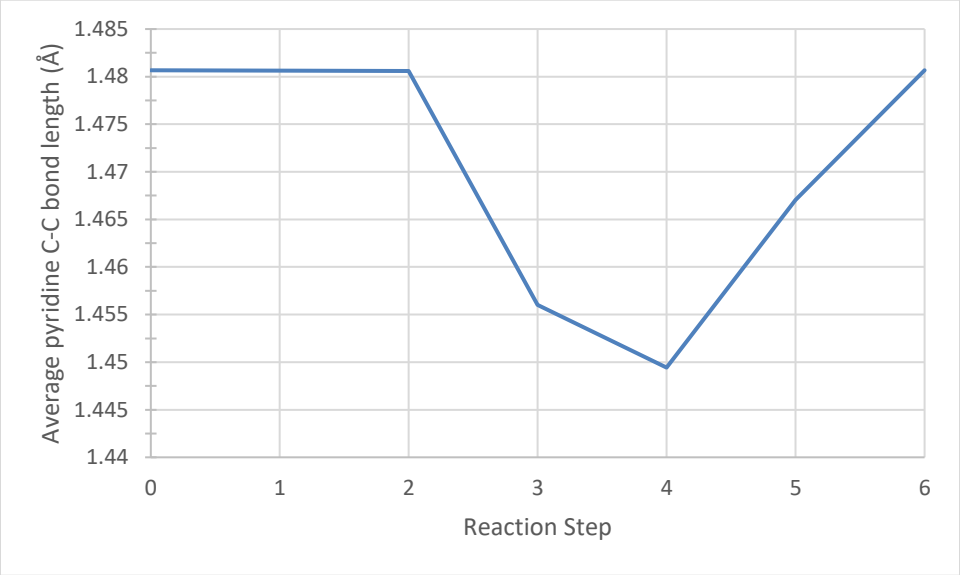

Figure 5.1: Average pyridine C-C bond length over reaction progress

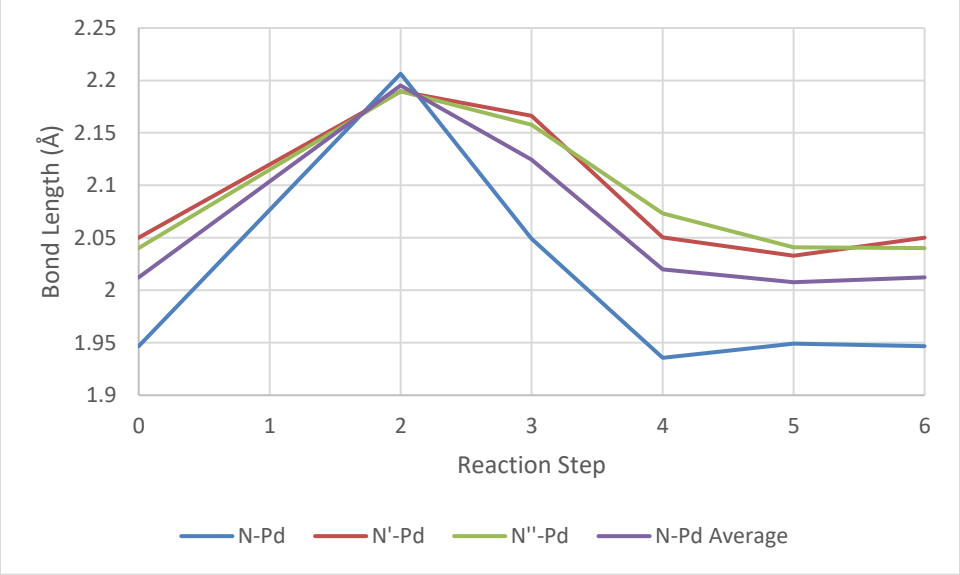

Figure 5.2: Pd-N bond lengths over reaction progress

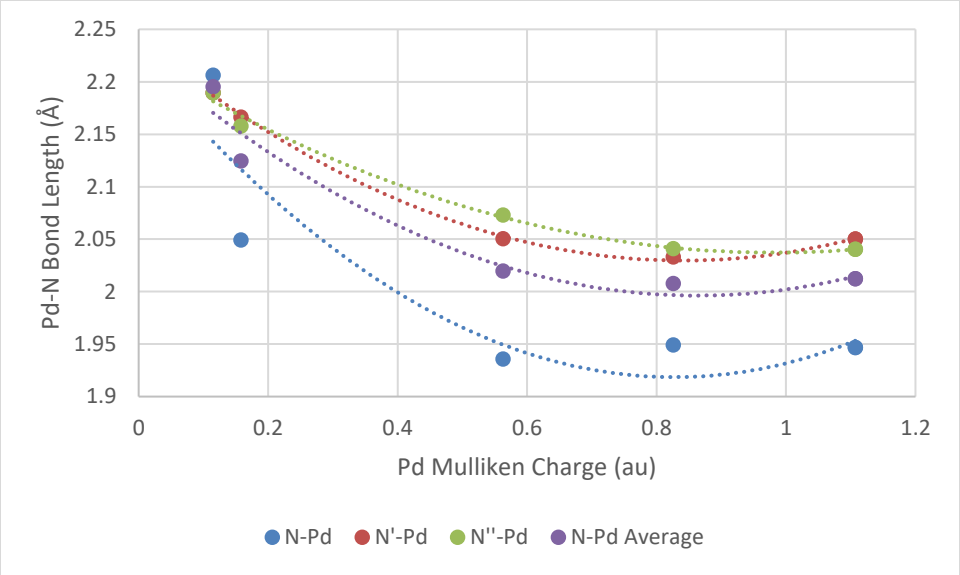

Figure 5.3: Pd-N bonds vs Pd Mulliken charge

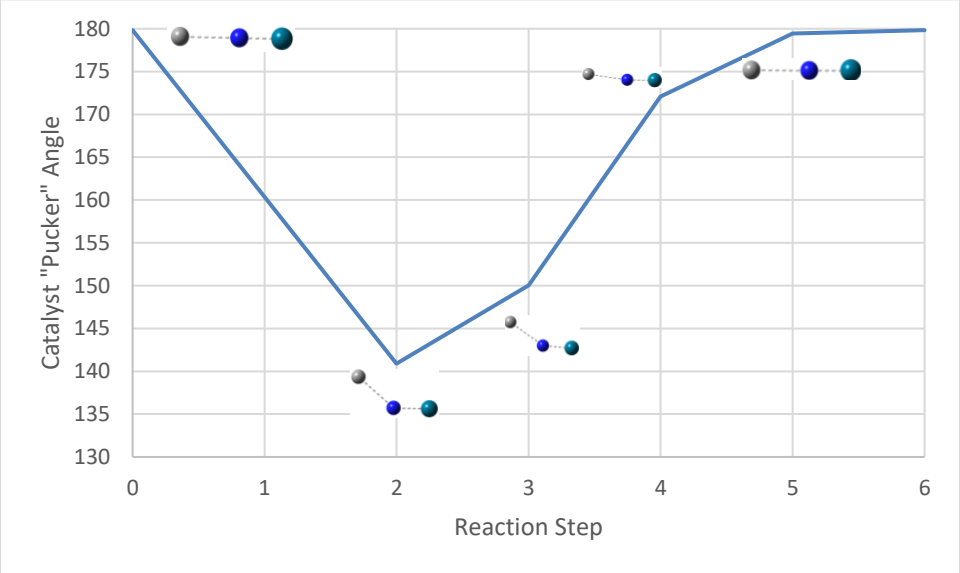

Figure 5.4: Catalyst "pucker" angle over reaction progress, images shown are side profile of Pd-N'-4'C

The energetic barrier for the formation of the reduced intermediate species is explained by the strained Pd-N bonds. As shown in

Figure 5.2, the Pd-N bonds increase by an average of 0.18Å relative to the original catalyst complex, accompanied by a 56.97 kcal/mol increase in energy. These bonds are lengthened in the intermediate geometry due to the reduced oxidation state on the Pd center, as the increased charge density repels the electronegative N centers in the terpyridine ligand. This is reflected in Figure 5.3, as the Pd-N average bond length increases as the charge density (reflected by the Mulliken charge) decreases.

Once the complex is in the $Pd^{(0)}$ intermediate state, the barrier for the hydrodeoxygenation part of the reaction is much lower (23.39 kcal/mol relative to the intermediate) than in the hydride pathways (53.91 kcal/mol and 55.48 kcal/mol for closed and open respectively). However, the high barrier for formation of the reduced intermediate compared to either of the hydride intermediates studied makes this pathway unfavorable.

5.2: Hydride Pathway

As discussed previously, two potential hydride intermediate pathways were investigated. The key difference between these two pathways is the geometry of the hydride intermediate (Figure 5.5). In the first pathway, the catalyst complex retains its original square planar geometry as shown in Figure 5.5 on the left. In the second pathway, however, the Pd-N and Pd-N' bonds within the complex are broken before the complex forms, allowing its terpyridine ring system to open. This leads to a significant decrease in energy in the formation of the hydride, as well as yielding a stabilized hydride intermediate as demonstrated by the energies shown in Figure 4.8. The observed stabilization effect comes from the protonation of the pyridyl nitrogen.

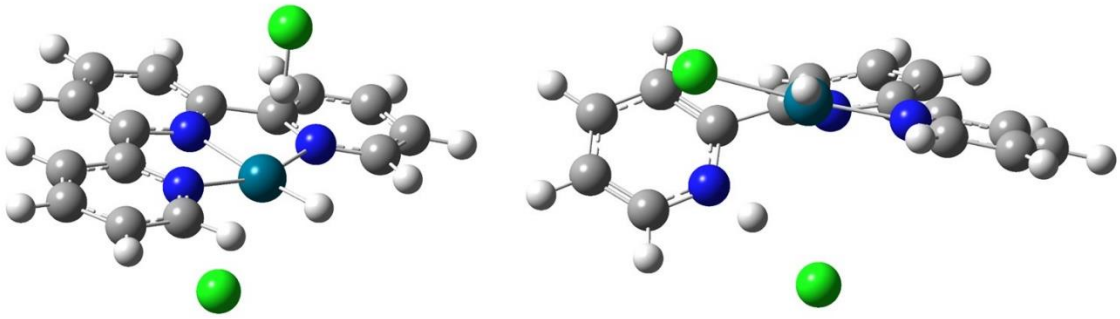

Figure 5.5: Comparison of closed (left) and open (right) hydride intermediate structures

By breaking the Pd-N and Pd-N' bonds and protonating the N atom, the structure is stabilized relative to the original complex, which has slightly strained Pd-N bonds. However, this stabilization does increase the activation barrier relative to the intermediate geometry. As described in section 4.2.3: the energy barrier between the intermediate and the RDS transition state is 1.57 kcal/mol higher in the open hydride pathway than in the closed hydride pathway. However, the barrier between the initial reactants and the RDS transition state is 19.74 kcal/mol lower in the open hydride than in the closed. Since the two intermediates are connected through the reactants, there will be an equilibrium between the intermediates that will favor the open pathway intermediate. From the open intermediate, the reaction can either proceed forward through the open RDS or backwards through the closed pathway, and likewise the closed intermediate can proceed forward through the closed RDS or backwards through the open pathway. Since the barrier from the closed intermediate through the open pathway is lower than the barrier through the closed pathway, the open hydride pathway will likely be favored. However, this should be verified experimentally.

5.3: Comparison of Pathways

Based on the energies shown above in Figure 4.9, we can see that the reductive pathway is notably higher in activation energy than either of the hydride pathways, and that the open hydride pathway is significantly lower in activation energy than the closed hydride pathways. This trend is due to the increased energy penalty for the reduction of the Pdtpy complex. In the reduced complex, the three Pd-N bonds are strained by an average 0.18Å relative to the initial $Pd^{(II)}$tpy complex (Table 4.1), compared to an average strain of 0.05Å in the closed hydride intermediate and a Pd-N'' bond strain of 0.02Å in the open hydride intermediate. Because we do not observe this same degree bond strain in the hydride complexes, the intermediate energies are significantly lower. This is consistent with the hydride intermediate proposed by Yao and coworkers[14] with their ruthenium complex for the HDO of vanillyl alcohol.

5.4: Impact of Solvation

We initially assumed that the use of a nonpolar solvent would have negligible effect on the overall reaction energy in relation to the gas phase energy. Surprisingly, as shown in Figure 4.1, Figure 4.6, and Figure 4.7, there is a noticeable (3-28 kcal/mol) increase in energy in the n-dodecane calculations compared to the gas phase calculations. The difference between the gas and solvated energies is significantly larger in the reductive pathway than in the hydride pathways, likely due to the relative instability of the hydroxyl anion produced by the hydride RDS in an apolar environment and the stability of the product of the reductive pathway RDS before the protonation step.

As noted in Table 1.1, the Vannucci group tested several solvents before determining that the optimal reaction conditions occurred in n-dodecane with the silica-supported catalyst complex. However, given the increase in activation energy upon the addition of solvent effects from n-dodecane, it is possible that another solvent could have a lower activation energy for the reaction. It is also possible that the silica surface, which was not considered in this project, could have a significant stabilizing effect on the reaction in dodecane.

5.5: Experimental Considerations

Due to the extremely high barrier for the formation of the reductive intermediate compared to the formation of the hydride intermediate species, it is likely that the hydride intermediate proposed in Delucia and coworkers' 2018 paper[1] is the correct intermediate. However, as two hydride intermediate geometries have been found computationally, experimental work might be done to determine which of these intermediates is likely to occur. To do this, the catalyst could be allowed to react with H_2 as in the HDO reaction explored originally,[2] but in the absence of the benzyl alcohol substrate. This would isolate the hydride intermediate species for characterization. After determining that this hydride intermediate is formed, it can then be allowed to react with the benzyl alcohol substrate to confirm that the intermediate does produce the correct products.

Chapter 6: Conclusion

6.1: Summary of Work

The goal of this work was to determine the reaction pathway for the HDO of benzyl alcohol with the Pdtpy catalyst developed by the Vannucci group.[1,2,6] As they were experimentally unsuccessful at isolating the intermediate species, we investigated the reaction using DFT simulations to determine which of the proposed intermediate species corresponded to a more favorable pathway.

We found that the proposed reductive intermediate pathway had an activation energy of 80.36 kcal/mol. The proposed hydride pathway we determined could occur through either a closed hydride intermediate or an open hydride intermediate in which one of the pyridyl nitrogen atoms dissociated from the metal center to be protonated after the hydride formation step. The closed hydride pathway had an activation energy of 66.03 kcal/mol, and the open hydride pathway had an activation energy of 46.29 kcal/mol. The energy determined for the reductive intermediate pathway show that it is significantly disfavored over either of the hydride intermediate structures. Based on these activation energies, the intermediate could be experimentally isolated by allowing the catalyst to react with H_2 in solution in the absence of the substrate, then rapidly cooling the catalyst to ensure that the reaction cannot continue. The intermediate formation is not dependent on the presence of the substrate, and as shown in Figure 4.9, the intermediate (step 3) is far lower in energy than the RDS transition state energy (step 5). This would allow the isolation and detection of the intermediate species, which could then be characterized experimentally as discussed in section 5.5: .

6.2: Future Work

In the development of this catalyst, the Vannucci group has found the optimal reaction conditions by attaching the catalyst to an amorphous silica surface.[1,2,6] For this project, we do not consider the effect of the silica surface on the reaction pathway in order to decrease the computational cost of the calculations discussed. As shown in Figure 1.5, the catalyst complex is believed to interact with the silica surface by lying parallel to the surface.[7] This catalyst-surface interaction could have an impact on the reaction energies. Because the catalyst is thought to lie parallel to the silica surface, the additional steric hindrance could negatively impact the open hydride reaction pathway, as the pyridine ring system opens in the opposite direction of the HDO process. The catalyst complex is bound to the silica surface by a carboxyl group on the 4' carbon. This carboxyl group would have some electron-withdrawing effect on the terpyridine system, which could affect the overall reaction pathway of the complex. The effects of this carboxyl group and of the silica surface should be considered in future work, as should the potential impact of other nearby catalyst complexes. Delucia reports dense coverage of the surface with the catalyst complex,[2] which means that there are likely other catalyst complexes nearby that could have an impact on the favorability of one pathway over another.

Delucia and coworkers also report that this catalyst works for the HDO of benzaldehyde, benzophenone, vanillin, and vanillyl alcohol.[2] Future computational work on this catalyst should investigate these substrates as well, as they could give improved insight as to the identity of the intermediate for this reaction.

References

(1) DeLucia, N. A.; Das, N.; Overa, S.; Paul, A.; Vannucci, A. K. Low Temperature Selective Hydrodeoxygenation of Model Lignin Monomers from a Homogeneous Palladium Catalyst. *Catal. Today* **2018**, *302*, 146–150. https://doi.org/10.1016/j.cattod.2017.05.050.

(2) DeLucia, N. A.; Jystad, A.; Laan, K. V.; Tengco, J. M. M.; Caricato, M.; Vannucci, A. K. Silica Supported Molecular Palladium Catalyst for Selective Hydrodeoxygenation of Aromatic Compounds under Mild Conditions. *ACS Catal.* **2019**, *9* (10), 9060–9071. https://doi.org/10.1021/acscatal.9b02460.

(3) Polcaro, A. M.; Dernini, M. S.; Palmas, S. Electrodeposition of Catalysts for Hydrogenation of Organic Molecules: Hydrogenation of Benzaldehyde. *Electrochimica Acta* **1992**, *37* (2), 365–367. https://doi.org/10.1016/0013-4686(92)85025-G.

(4) Polcaro, A. M.; Palmas, S.; Dernini, S. Role of Catalyst Characteristics in Electrocatalytic Hydrogenation: Reduction of Benzaldehyde and Acetophenone on Carbon Felt/Palladium Electrodes. *Ind. Eng. Chem. Res.* **1993**, *32* (7), 1315–1322. https://doi.org/10.1021/ie00019a005.

(5) Ruberu, T. P. A.; Nelson, N. C.; Slowing, I. I.; Vela, J. Selective Alcohol Dehydrogenation and Hydrogenolysis with Semiconductor-Metal Photocatalysts: Toward Solar-to-Chemical Energy Conversion of Biomass-Relevant Substrates. *J. Phys. Chem. Lett.* **2012**, *3* (19), 2798–2802. https://doi.org/10.1021/jz301309d.

(6) Jystad, A. Computational Characterization of Amorphous Silica Supported Catalysts, University of Kansas, 2020.

(7) Kaihua Zhang; Katherine Vander Laan. Unpublished Private Communication, 2020.

(8) Bu, Q.; Lei, H.; Zacher, A. H.; Wang, L.; Ren, S.; Liang, J.; Wei, Y.; Liu, Y.; Tang, J.; Zhang, Q.; Ruan, R. A Review of Catalytic Hydrodeoxygenation of Lignin-Derived Phenols from Biomass Pyrolysis. *Bioresour. Technol.* **2012**, *124*, 470–477. https://doi.org/10.1016/j.biortech.2012.08.089.

(9) Ju, C.; Li, M.; Fang, Y.; Tan, T. Efficient Hydro-Deoxygenation of Lignin Derived Phenolic Compounds over Bifunctional Catalysts with Optimized Acid/Metal Interactions. *Green Chem.* **2018**, *20* (19), 4492–4499. https://doi.org/10.1039/C8GC01960F.

(10) Saidi, M.; Samimi, F.; Karimipourfard, D.; Nimmanwudipong, T.; Gates, B. C.; Rahimpour, M. R. Upgrading of Lignin-Derived Bio-Oils by Catalytic Hydrodeoxygenation. *Energy Env. Sci* **2014**, *7* (1), 103–129. https://doi.org/10.1039/C3EE43081B.

(11) Su-Ping, Z. Study of Hydrodeoxygenation of Bio-Oil from the Fast Pyrolysis of Biomass. *Energy Sources* **2003**, *25* (1), 57–65. https://doi.org/10.1080/00908310290142118.

(12) Nolte, M. W.; Shanks, B. H. A Perspective on Catalytic Strategies for Deoxygenation in Biomass Pyrolysis. *Energy Technol.* **2017**, *5* (1), 7–18. https://doi.org/10.1002/ente.201600096.

(13) Si, Z.; Zhang, X.; Wang, C.; Ma, L.; Dong, R. An Overview on Catalytic Hydrodeoxygenation of Pyrolysis Oil and Its Model Compounds. *Catalysts* **2017**, *7* (6), 169. https://doi.org/10.3390/catal7060169.

(14) Yao, W.; Das, S.; DeLucia, N. A.; Qu, F.; Boudreaux, C. M.; Vannucci, A. K.; Papish, E. T. Determining the Catalyst Properties That Lead to High Activity and Selectivity for

Catalytic Hydrodeoxygenation with Ruthenium Pincer Complexes. *Organometallics* **2020**, *39* (5), 662–669. https://doi.org/10.1021/acs.organomet.9b00816.
(15) Gilkey, M. J.; Xu, B. Heterogeneous Catalytic Transfer Hydrogenation as an Effective Pathway in Biomass Upgrading. *ACS Catal.* **2016**, *6* (3), 1420–1436. https://doi.org/10.1021/acscatal.5b02171.
(16) Gao, D.; Xiao, Y.; Varma, A. Guaiacol Hydrodeoxygenation over Platinum Catalyst: Reaction Pathways and Kinetics. *Ind. Eng. Chem. Res.* **2015**, *54* (43), 10638–10644. https://doi.org/10.1021/acs.iecr.5b02940.
(17) Chiu, C.; Genest, A.; Borgna, A.; Rösch, N. Hydrodeoxygenation of Guaiacol over Ru(0001): A DFT Study. *ACS Catal.* **2014**, *4* (11), 4178–4188. https://doi.org/10.1021/cs500911j.
(18) Gutierrez, A.; Kaila, R. K.; Honkela, M. L.; Slioor, R.; Krause, A. O. I. Hydrodeoxygenation of Guaiacol on Noble Metal Catalysts. *Catal. Today* **2009**, *147* (3–4), 239–246. https://doi.org/10.1016/j.cattod.2008.10.037.
(19) Lu, J.; Heyden, A. Theoretical Investigation of the Reaction Mechanism of the Hydrodeoxygenation of Guaiacol over a Ru(0 0 0 1) Model Surface. *J. Catal.* **2015**, *321*, 39–50. https://doi.org/10.1016/j.jcat.2014.11.003.
(20) Peters, J. E.; Carpenter, J. R.; Dayton, D. C. Anisole and Guaiacol Hydrodeoxygenation Reaction Pathways over Selected Catalysts. *Energy Fuels* **2015**, *29* (2), 909–916. https://doi.org/10.1021/ef502551p.
(21) Verma, A. M.; Kishore, N. DFT Analyses of Reaction Pathways and Temperature Effects on Various Guaiacol Conversion Reactions in Gas Phase Environment. *ChemistrySelect* **2016**, *1* (19), 6196–6205. https://doi.org/10.1002/slct.201601139.
(22) Zhou, M.; Wang, Y.; Wang, Y.; Xiao, G. Catalytic Conversion of Guaiacol to Alcohols for Bio-Oil Upgrading. *J. Energy Chem.* **2015**, *24* (4), 425–431. https://doi.org/10.1016/j.jechem.2015.06.012.
(23) Lee, K.; Gu, G. H.; Mullen, C. A.; Boateng, A. A.; Vlachos, D. G. Guaiacol Hydrodeoxygenation Mechanism on Pt(111): Insights from Density Functional Theory and Linear Free Energy Relations. *ChemSusChem* **2015**, *8* (2), 315–322. https://doi.org/10.1002/cssc.201402940.
(24) Lien, C.-H.; Medlin, J. W. Promotion of Activity and Selectivity by Alkanethiol Monolayers for Pd-Catalyzed Benzyl Alcohol Hydrodeoxygenation. *J. Phys. Chem. C* **2014**, *118* (41), 23783–23789. https://doi.org/10.1021/jp507114g.
(25) Bouxin, F. P.; Zhang, X.; Kings, I. N.; Lee, A. F.; Simmons, M. J. H.; Wilson, K.; Jackson, S. D. Mechanistic Aspects of Hydrodeoxygenation of *p* -Methylguaiacol over Rh/Silica and Pt/Silica. *Org. Process Res. Dev.* **2018**, *22* (12), 1586–1589. https://doi.org/10.1021/acs.oprd.8b00211.
(26) Liu, C.; Shao, Z.; Xiao, Z.; Williams, C. T.; Liang, C. Hydrodeoxygenation of Benzofuran over Silica–Alumina-Supported Pt, Pd, and Pt–Pd Catalysts. *Energy Fuels* **2012**, *26* (7), 4205–4211. https://doi.org/10.1021/ef300694c.
(27) Yu, Y.; Gutiérrez, O. Y.; Haller, G. L.; Colby, R.; Kabius, B.; Rob van Veen, J. A.; Jentys, A.; Lercher, J. A. Tailoring Silica–Alumina-Supported Pt–Pd as Poison-Tolerant Catalyst for Aromatics Hydrogenation. *J. Catal.* **2013**, *304*, 135–148. https://doi.org/10.1016/j.jcat.2013.04.009.
(28) Yu, Y.; Fonfé, B.; Jentys, A.; Haller, G. L.; van Veen, J. A. R.; Gutiérrez, O. Y.; Lercher, J. A. Bimetallic Pt–Pd/Silica–Alumina Hydrotreating Catalysts – Part I: Physicochemical

Characterization. *J. Catal.* **2012**, *292*, 1–12. https://doi.org/10.1016/j.jcat.2012.03.017.
(29) Sergeev, A. G.; Hartwig, J. F. Selective, Nickel-Catalyzed Hydrogenolysis of Aryl Ethers. *Science* **2011**, *332* (6028), 439–443. https://doi.org/10.1126/science.1200437.
(30) Kusumoto, S.; Nozaki, K. Direct and Selective Hydrogenolysis of Arenols and Aryl Methyl Ethers. *Nat. Commun.* **2015**, *6* (1), 6296. https://doi.org/10.1038/ncomms7296.
(31) Szabo, A.; Ostlund, Neil. *Modern Quantum Chemistry: Introduction to Advanced Electronic Structure Theory*, First edition, revised.; Dover, 1996; Vol. 1.
(32) Foresman, James B.; Frisch, Aeleen. *Exploring Chemistry with Electronic Structure Methods*, Third edition.; Gaussian, Inc.
(33) Andrae, D.; Häußermann, U.; Dolg, M.; Stoll, H.; Preuß, H. Energy-Adjustedab Initio Pseudopotentials for the Second and Third Row Transition Elements. *Theor. Chim. Acta* **1990**, *77* (2), 123–141. https://doi.org/10.1007/BF01114537.
(34) Hohenberg, P.; Kohn, W. Inhomogeneous Electron Gas. *Phys. Rev.* **1964**, *136* (3B), B864–B871. https://doi.org/10.1103/PhysRev.136.B864.
(35) Johnson, E. R.; Mackie, I. D.; DiLabio, G. A. Dispersion Interactions in Density-Functional Theory. *J. Phys. Org. Chem.* **2009**, *22* (12), 1127–1135. https://doi.org/10.1002/poc.1606.
(36) Grimme, S.; Hansen, A.; Brandenburg, J. G.; Bannwarth, C. Dispersion-Corrected Mean-Field Electronic Structure Methods. *Chem. Rev.* **2016**, *116* (9), 5105–5154. https://doi.org/10.1021/acs.chemrev.5b00533.
(37) Kohn, W.; Sham, L. J. Self-Consistent Equations Including Exchange and Correlation Effects. *Phys. Rev.* **1965**, *140* (4A), A1133–A1138. https://doi.org/10.1103/PhysRev.140.A1133.
(38) Chai, J.-D.; Head-Gordon, M. Long-Range Corrected Hybrid Density Functionals with Damped Atom–Atom Dispersion Corrections. *Phys. Chem. Chem. Phys.* **2008**, *10* (44), 6615. https://doi.org/10.1039/b810189b.
(39) Grimme, S.; Antony, J.; Schwabe, T.; Mück-Lichtenfeld, C. Density Functional Theory with Dispersion Corrections for Supramolecular Structures, Aggregates, and Complexes of (Bio)Organic Molecules. *Org. Biomol. Chem.* **2007**, *5* (5), 741–758. https://doi.org/10.1039/B615319B.
(40) Gräfenstein, J.; Cremer, D. An Efficient Algorithm for the Density-Functional Theory Treatment of Dispersion Interactions. *J. Chem. Phys.* **2009**, *130* (12), 124105. https://doi.org/10.1063/1.3079822.
(41) Grimme, S. Semiempirical GGA-type density functional constructed with a long-range dispersion correction. *J. Comput. Chem.* **2006**, *27* (15), 1787–1799. https://doi.org/10.1002/jcc.20495.
(42) Chai, J.-D.; Head-Gordon, M. Systematic Optimization of Long-Range Corrected Hybrid Density Functionals. *J. Chem. Phys.* **2008**, *128* (8), 084106. https://doi.org/10.1063/1.2834918.
(43) Marenich, A. V.; Cramer, C. J.; Truhlar, D. G. Universal Solvation Model Based on Solute Electron Density and on a Continuum Model of the Solvent Defined by the Bulk Dielectric Constant and Atomic Surface Tensions. *J. Phys. Chem. B* **2009**, *113* (18), 6378–6396. https://doi.org/10.1021/jp810292n.

(44) Cancès, E.; Mennucci, B.; Tomasi, J. A New Integral Equation Formalism for the Polarizable Continuum Model: Theoretical Background and Applications to Isotropic and Anisotropic Dielectrics. *J. Chem. Phys.* **1997**, *107* (8), 3032–3041. https://doi.org/10.1063/1.474659.
(45) Mennucci, B.; Tomasi, J. Continuum Solvation Models: A New Approach to the Problem of Solute's Charge Distribution and Cavity Boundaries. *J. Chem. Phys.* **1997**, *106* (12), 5151–5158. https://doi.org/10.1063/1.473558.
(46) Mennucci, B.; Cancès, E.; Tomasi, J. Evaluation of Solvent Effects in Isotropic and Anisotropic Dielectrics and in Ionic Solutions with a Unified Integral Equation Method: Theoretical Bases, Computational Implementation, and Numerical Applications. *J. Phys. Chem. B* **1997**, *101* (49), 10506–10517. https://doi.org/10.1021/jp971959k.
(47) Schlegel, H. B. Optimization of Equilibrium Geometries and Transition Structures. *J. Comput. Chem.* **1982**, *3* (2), 214–218. https://doi.org/10.1002/jcc.540030212.
(48) Fukui, K. The Path of Chemical Reactions - the IRC Approach. *Acc. Chem. Res.* **1981**, 6.
(49) Becke, A. D. Density-Functional Thermochemistry. V. Systematic Optimization of Exchange-Correlation Functionals. *J. Chem. Phys.* **1997**, *107* (20), 8554–8560. https://doi.org/10.1063/1.475007.
(50) Becke, A. D. Density-functional Thermochemistry. III. The Role of Exact Exchange. *J. Chem. Phys.* **1993**, *98* (7), 5648–5652. https://doi.org/10.1063/1.464913.
(51) Grimme, S.; Antony, J.; Ehrlich, S.; Krieg, H. A Consistent and Accurate *Ab Initio* Parametrization of Density Functional Dispersion Correction (DFT-D) for the 94 Elements H-Pu. *J. Chem. Phys.* **2010**, *132* (15), 154104. https://doi.org/10.1063/1.3382344.
(52) Frisch, M. J.; Trucks, G. W.; Cheeseman, J. R.; Scalmani, G.; Caricato, M.; Hratchian, H. P.; Li, X.; Barone, V.; Bloino, J.; Zheng, G.; Vreven, T.; Montgomery, J. A.; Petersson, G. A.; Scuseria, G. E.; Schlegel, H. B.; Nakatsuji, H.; Izmaylov, A. F.; Martin, R. L.; Sonnenberg, J. L.; Peralta, J. E.; Heyd, J. J.; Brothers, E.; Ogliaro, F.; Bearpark, M.; Robb, M. A.; Mennucci, B.; Kudin, K. N.; Staroverov, V. N.; Kobayashi, R.; Normand, J.; Rendell, A.; Gomperts, R.; Zakrzewski, V. G.; Hada, M.; Ehara, M.; Toyota, K.; Fukuda, R.; Hasegawa, J.; Ishida, M.; Nakajima, T.; Honda, Y.; Kitao, O.; Nakai, H. *Gaussian Development Version, Revision J.13*.
(53) Weigend, F.; Ahlrichs, R. Balanced Basis Sets of Split Valence, Triple Zeta Valence and Quadruple Zeta Valence Quality for H to Rn: Design and Assessment of Accuracy. *Phys. Chem. Chem. Phys.* **2005**, *7* (18), 3297–3305. https://doi.org/10.1039/B508541A.
(54) Schäfer, A.; Huber, C.; Ahlrichs, R. Fully Optimized Contracted Gaussian Basis Sets of Triple Zeta Valence Quality for Atoms Li to Kr. *J. Chem. Phys.* **1994**, *100* (8), 5829–5835. https://doi.org/10.1063/1.467146.